Modeling proton exchange membrane fuel cells with fiber-based microporous layers

P.Z. Lin[a,1], J. Sun[a,1], M.H. Shao[b,e], M.C. Wu[c,*], T.S. Zhao[a,d,*]

[a] Department of Mechanical and Aerospace Engineering, The Hong Kong University of Science and Technology, Clear Water Bay, Kowloon, Hong Kong SAR, China

[b] Department of Chemical and Biological Engineering, The Hong Kong University of Science and Technology, Clear Water Bay, Kowloon, Hong Kong SAR, China

[c] Department of Mechanical Engineering, The Hong Kong Polytechnic University, Hung Hom, Kowloon, Hong Kong SAR, China

[d] Guangzhou HKUST Fok Ying Tung Research Institute, Guangzhou, 511458, China

[e] Energy Institute, The Hong Kong University of Science and Technology, Clear Water Bay, Kowloon, Hong Kong SAR, China

Abstract

Microporous layers (MPLs) play a crucial role in improving water management in proton exchange membrane fuel cells (PEMFCs). Highly tunable electrospun carbon fibers offer a promising candidate for MPLs to facilitate two-phase water and gas transport in PEMFCs. In this work, we present a two-phase PEMFC model to investigate the mass transport characteristics in MPLs made of nano-/micro-fibers. Simulations were validated by the reported experimental results. It is revealed that the fiber-based MPLs (fMPLs) reduce the liquid water saturation at the cathode side due to the higher permeability, thus significantly reducing the oxygen transport resistance and resulting in superior cell performance than conventional MPLs (cMPLs) do. Moreover, PEMFCs with fMPLs outperform those with

* Corresponding authors
E-mail addresses:
maochun.wu@polyu.edu.hk (M.C. Wu), zhaots@sustech.edu.cn (T.S. Zhao).
[1] These authors contributed equally to this work.

cMPLs under a wide range of operating temperatures from 40 to 80 ℃. In addition, our parametric study results suggest that fMPLs with a high porosity (> 0.5), a large fiber diameter (> 2 μm), and a large contact angle (> 135°) can effectively boost water drainage and gas transport, thereby considerably enhancing the PEMFC performance. This work provides insights into the two-phase transport behavior in PEMFCs with fMPLs, paving the way for design and development of novel MPLs for high-performance PEMFCs.

Keywords: Proton exchange membrane fuel cell; microporous layer; two-phase model; electrospun carbon fibers; water management

Nomenclature

List of symbols

A	Specific surface area
C	Molar concentration
D	Diffusivity
F	Faraday's constant
H	Henry's constant
i	Current density
i_0^{ref}	Reference exchange current density
J	Electrochemical reaction rate
j	Flux
K	Permeability
k_r	Relative permeability
k_{ads}	Adsorption rate
k_{des}	Desorption rate
k_{eva}	Evaporation rate
k_{con}	Condensation rate
M	Molar mass
m_{Pt}	Pt loading
n_d	Electro-osmotic drag coefficient
p	Pressure
p_c	Capillary pressure
S	Source term
s	Liquid water saturation
T	Temperature

Superscripts

eff	Effective value
ref	Reference value

Greek symbols

α	Transfer coefficient
γ	Reaction order
δ	Thickness
ε	Porosity or volume fraction
η	Overpotential
θ_c	Contact angle
κ	Conductivity
λ	Membrane water content
μ	Dynamic viscosity
ρ	Density
τ	Tortuosity
ϕ	Potential
ω	Mass fraction

Subscripts

a	Anode
c	Cathode
CL	Catalyst layer
MPL	Microporous layer
BL	Backing layer
GDL	Gas diffusion layer
PEM	Proton exchange membrane
l	Liquid phase
g	Gas phase
i	Gas species i
ion	Ionomer
ec	Evaporation and condensation
ad	Adsorption and desorption
e	Electron
p	Proton
agg	Agglomerate

1. Introduction

Proton exchange membrane fuel cells (PEMFCs), featuring zero emissions and high efficiency, are one of the most promising clean power sources for combating energy crisis and environmental issues [1–4]. However, the wide commercial application of this technology is hindered by high cost and insufficient durability. Increasing power density represents an effective approach to reduce the stack size and thus capital cost of PEMFCs. However, enhancing the operating current density would generate a large amount of water in the cathode side, leading to the water flooding phenomenon that not only results in a catastrophic decrease in the power density but also deteriorates the durability of PEMFCs [5]. Hence, prompting water removal is crucial for PEMFCs to achieve high power densities, especially under high relative humidity.

To this end, a microporous layer (MPL), typical MPL is a thin layer made of carbon powders and polytetrafluorethylene (PTFE) [6], is usually incorporated into the gas diffusion layer (GDL), which keeps the membrane hydrated while facilitating water removal out of the catalyst layer (CL) [7–9]. Additional functions of MPLs include providing electrical contact between CL and backing layer (BL) and mechanical support. Both experiments [10–13] and simulations [14–16] have proved that MPL boosts water drainage. Great attention has been attached to design parameters of MPLs, including microstructure modification (e.g., porosity and pore size distribution) and surface engineering (e.g., morphology and wettability). In addition to the design optimization of the conventional MPL (cMPL), many other carbon materials, such as multiwall carbon nanotubes (MWCNT) [17–19] and graphene [20] have been used for fabricating MPLs. The unique morphology of the one-dimensional MWCNT and graphene nanoplatelets can increase the porosity of MPLs, thus boosting water and gas transport. Recently, electrospun carbon nanofibers were proposed as a promising MPL for PEMFCs due

to their highly tunable porous structures [21–23]. For example, Li et al. fabricated an electrospun MPL with fiber diameter of ~550 nm and contact angle of 135°, enabling the PEMFC to outperform that with conventional MPL at 70 ℃ under high relative humidity due to substantial reduction in mass transport losses [23]. The electrospun fibers can interweave into an integral, cracked-free layer with continuous porous structure. More attractively, the fiber diameter, porosity, hydrophobicity, and thickness can be well controlled by carefully adjusting the electrospinning parameters [24]. However, searching for optimal geometric properties of electrospun MPL through trial and error is labor- and time-consuming.

Numerical modeling offers an efficient tool for investigating the effects of various design and operating parameters on PEMFC performance [8,25]. In the early stage, the influence of temperature is neglected. Weber and Newman developed a two-phase, isothermal model and quantified the function of MPL in water management: membrane hydration and minimizing water flooding [15]. However, results based on the in situ synchrotron X-ray radiography experiments and coupled heat and mass transport model suggested that the impact of temperature was non-negligible [26]. To investigate the effect of temperature distribution on water transport in PEMFC, a one-dimensional non-isothermal two-phase model was built, which revealed the key role of phase-change-induced flow at high temperature [27]. In addition, Zhou et al. reported that the thermal conductivity of MPL was one of the determining parameters in improving vapor water diffusion and back diffusion, as MPL enhanced temperature gradient in CL, and thus improving vapor water diffusion and back diffusion [28]. However, experimental and numerical results suggested that the influence of the thermal conductivity was overestimated [29]. Instead, the structure of GDL was more critical. The effect of structure can be elucidated by using pore-scale models [25,30,31]. A two-phase pore-scale model incorporated with interfacial voids indicated that the morphology of MPL had a

significant effect on cell performance particularly under high current density [32] and suggested that cracks in MPL provided additional path for liquid water transport [14]. Unfortunately, cracks are detrimental to the mechanical durability [8,9]. Therefore, many new MPL structures have been proposed and fiber-based MPLs show great potential due to its superior mechanical durability and continuous porous structure [22,23,29]. However, the transport phenomena within PEMFCs using fiber-based MPLs are not fully understood. Moreover, the effects on design and operating parameters on the transport characteristics and cell performance remain to be explored.

In this work, we developed a two-phase multi-physics model for PEMFCs with fiber-based MPLs, which considered water transport in porous electrodes, membrane, and ionomer. The permeability of fMPL was described by Carman-Kozeny equation and the model was first validated by the reported experimental results. PEMFCs with fMPL and cMPL were compared to reveal the advantages of fMPL. In addition, the effects of different fMPL structural parameters, including porosity, fiber diameter, and contact angle were numerically investigated and optimized.

2. Model development

2.1. Computational domains and assumptions

As shown in Fig. 1a, the cMPL is made of carbon nanoparticles with hydrophobic treatment, which typically exhibits small pores of around 100 nm. The randomly packed powder MPL may result in a high tortuosity and even dead-end pores, which is prone to cause higher liquid water content in porous media and lead to water flooding that is fatal for PEMFCs. In contrast, the microstructure of electrospun microporous layers can be properly adjusted by controlling the electrospinning conditions. As shown in Fig. 1b, the interconnected pore network with

adjustable pore sizes can facilitate water drainage, alleviating the water flooding under high current densities and promoting oxygen transport, thus leading to high power densities. The two-phase model involves two-phase flow of liquid water and gas species in cathode porous media, while only gas transport is considered in the anode porous media. Fig. 1c presents the two-dimensional rib-channel cross-section computational domains of PEMFCs, including BLs, MPLs, CLs and proton exchange membrane (PEM). Geometric parameters and related physical parameters are given in Table 1.

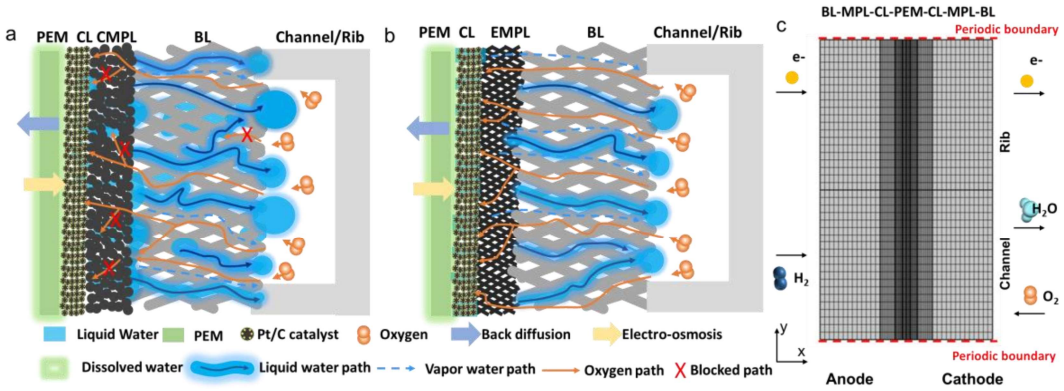

Fig. 1. Schematic of PEMFCs and computational domain. PEMFCs with (a) cMPL. (b) fMPL. (c) Computational domains.

For the sake of simplicity in this numerical study, assumptions are made as follows:

(1) A two-dimensional two-phase multi-physics model under steady-state conditions is considered, and the liquid water flow is only considered in the cathode.

(2) Gas species are assumed as continuous, incompressible, and ideal fluids.

(3) Porous electrodes, including CLs, MPLs, and BLs, are assumed as homogeneous porous media.

(4) Water generated by oxygen reduction reaction is considered as dissolved water in the ionomer of cathode CLs.

(5) Contact resistances between each layer are neglected.

Table 1 Parameters of PEMFC model [23,33,34].

	GDL	cMPL	fMPL	CL	PEM
Thickness [μm]	200	50	50	25	25
Porosity [-]	0.75	0.3	0.4	0.3	-
Tortuosity [-]	3	1.5	1.5	1.5	-
Permeability [m^2]	6×10^{-12}	5×10^{-15}	3.2×10^{-14}	1×10^{-13}	-
Thermal conductivity [$W\ m^{-1}\ K^{-1}$]	1	1	1	0.27	0.95

2.2. Mass transport

The governing equations for describing two-phase flow phenomena in porous media of PEMFCs include mass conservation, momentum conservation, and energy conservation [25,33,35], which are respectively described as:

$$\nabla \cdot (\rho \vec{u}) = S_m \tag{1}$$

$$\vec{u} = -K \frac{k_r}{\mu} \nabla p \tag{2}$$

$$\varepsilon \rho C_p \vec{u} \nabla \mathrm{T} = \nabla \cdot \left(k^{eff} \nabla T \right) + S_T \tag{3}$$

where $\vec{u}$ is velocity, ρ is density, μ is viscosity, ε is porosity, C_p is specific heat capacity, and T is temperature. K and k_r are permeability of porous media and relative permeability. S_m and S_T are the mass source and thermal source, respectively, which are given in Table 2.

The mass fractions of gas species in the porous electrodes can be obtained by solving the Stefan-Maxwell equations, given by [36]:

$$\nabla \cdot \left[-\rho \omega_i \sum_{j=1}^{N} D_{ij}^{eff} \frac{M_{total}}{M_j} \left(\nabla \omega_j + \omega_j \frac{\nabla M_{total}}{M_{total}} \right) \right] = S_i \tag{4}$$

where ω_i is mass fraction of gas species i, S_i is the corresponding source item of electrochemical reactions, D_{ij}^{eff} is the effective mixture diffusion coefficient, which is given by [36]:

$$D_{ij}^{eff} = \begin{cases} \dfrac{\varepsilon}{\tau}(1-s)^3 D_{ij} & \text{in MPLs, BLs} \\ \left(\dfrac{1}{D_{ij}} + \dfrac{1}{D_{i,Kn}} \right)^{-1} & \text{in CLs} \end{cases} \tag{5}$$

$$D_{ij} = \frac{\dfrac{\omega_i\left(\omega_j+\omega_k\right)}{x_i \tilde{D}_{jk}} + \dfrac{\omega_j\left(\omega_i+\omega_k\right)}{x_j \tilde{D}_{ik}} - \dfrac{\omega_k^2}{x_k \tilde{D}_{ij}}}{\dfrac{x_i}{\tilde{D}_{ij}\tilde{D}_{ik}} + \dfrac{x_j}{\tilde{D}_{ij}\tilde{D}_{jk}} + \dfrac{x_k}{\tilde{D}_{ik}\tilde{D}_{jk}}} \tag{6}$$

$$D_{i,Kn} = \frac{d_p}{3}\sqrt{\frac{8RT}{\pi M_i}} \tag{7}$$

where ε and τ are the porosity and tortuosity of porous media, s is the liquid water saturation. D_{ij} is the mixture diffusion coefficient, $D_{i,Kn}$ is Knudsen diffusion coefficient, $\tilde{D}_{ij}$ is the binary diffusion coefficient. i, j, and k denote types of gas species. x_i is the molar fraction of gas species i. d_p is the pore diameter of porous media, and M_i is the molar mass of gas species i.

Table 2 Source terms of conservation equations.

	Expression	Area
S_{O_2}	$\begin{cases} -J_c / 4F \\ 0 \end{cases}$	in cCL in cMPL, cBL
S_{H_2}	$\begin{cases} -J_a / 2F \\ 0 \end{cases}$	in aCL in aMPL, aBL

$$
S_{H_2O} = \begin{cases} -S_{ec} & \text{in cMPL, cBL} \\ -S_{ec} - S_{ad} & \text{in cCL} \\ -S_{ad} & \text{in aCL} \\ 0 & \text{in aMPL, aBL} \end{cases}
$$

$$
S_s = \begin{cases} S_{ec} + (1-\omega) J_c / 2F & \text{in cCL} \\ S_{ec} & \text{in cMPL, cBL} \end{cases}
$$

$$
S_T = \begin{cases} j_e^2 / \kappa_e + H_{ec} S_{ec} & \text{in cMPL, cBL} \\ j_e^2 / \kappa_e + j_p^2 / \kappa_p + H_{ad} S_{ad} + H_{ec} S_{ec} & \text{in cCL} \\ j_p^2 / \kappa_p & \text{in PEM} \\ j_e^2 / \kappa_e + j_p^2 / \kappa_p + H_{ad} S_{ad} & \text{in aCL} \\ j_e^2 / \kappa_e & \text{in aMPL, aBL} \end{cases}
$$

$$
S_e = \begin{cases} -J_c / 4F & \text{in cCL} \\ 0 & \text{in cMPL, cBL} \end{cases}
$$

$$
S_p = \begin{cases} -J_c / 4F & \text{in cCL} \\ 0 & \text{in cMPL, cBL} \end{cases}
$$

$$
S_\lambda = \begin{cases} S_{ad} + \omega J_c / 2F & \text{in cCL} \\ 0 & \text{in PEM} \\ S_{ad} & \text{in aCL} \end{cases}
$$

Evaporation and condensation equations are applied to calculate the phase change between liquid and vapor water. Evaporation and condensation sources are given by [37,38]:

$$
S_{ec} = \begin{cases} \dfrac{k_{eva} a_{lg} s (p_{H_2O} - p_{sat})}{RT} & \text{if } p_{H_2O} < p_{sat} \text{ (evaporation)} \\ \dfrac{k_{con} a_{lg} (1-s)(p_{H_2O} - p_{sat})}{RT} & \text{if } p_{H_2O} > p_{sat} \text{ (condensation)} \end{cases} \tag{8}
$$

where p_{sat} is the saturation pressure of water, p_{H_2O} is the partial pressure of water, a_{lg} is the effective scaling factor between liquid and gas, k_{eva} and k_{con} are rates of water evaporation and condensation.

Water transport in membrane and ionomer is determined by back diffusion and electro-osmosis [37]:

$$\nabla \cdot \left(-\frac{D_\lambda}{\mathrm{V}_m} \nabla \lambda + \frac{n_d}{F} j_p \right) = S_m \tag{9}$$

where D_λ is the effective water diffusivity in the ionomer, V_m is equivalent molar volume of the ionomer, λ is the water content of ionomer, and n_d is the electro-osmotic drag coefficient.

Water content dissolved in ionomer can be described by adsorption and desorption [37]:

$$S_{ad} = \begin{cases} \dfrac{k_{\mathrm{ads}}}{\delta_{CL} V_{\mathrm{m}}} \left(\lambda_{\mathrm{eq}} - \lambda \right) & \text{if } \lambda < \lambda_{\mathrm{eq}} \text{ (absorption)} \\ \dfrac{k_{des}}{\delta_{CL} V_{\mathrm{m}}} \left(\lambda_{\mathrm{eq}} - \lambda \right) & \text{if } \lambda > \lambda_{\mathrm{eq}} \text{ (desorption)} \end{cases} \tag{10}$$

where λ_{eq} is the equilibrium water content of the ionomer, δ_{CL} is the thickness of CL, k_{ads} and k_{des} are rates of water adsorption and desorption.

For the liquid water in porous media in cathode, its flow is driven by capillary pressure, which is given by [39]:

$$p_c = p_g - p_l = \sigma \cos\theta_c (\varepsilon / K)^{0.5} J(s) \tag{11}$$

$$J(s) = \begin{cases} 1.417(1-s) - 2.120(1-s)^2 + 1.263(1-s)^3 & 0 < \theta_c < 90^\circ \\ 1.417s - 2.120s^2 + 1.263s^3 & 90^\circ < \theta_{\mathrm{c}} < 180^\circ \end{cases} \tag{12}$$

where σ is surface tension coefficient, θ_c is the contact angle of porous media, $J(s)$ is the Leverette function with liquid water saturation [40]. K is the permeability of porous media, which is given by [39]:

$$K = k_{abs} k_r = \begin{cases} k_{abs} s^3, & \text{liquid} \\ k_{abs} (1-s)^3, & \text{gas} \end{cases} \tag{13}$$

where k_{abs} is the absolute permeability and k_r is the relative permeability used for describing two-phase flow in porous media.

To investigate the effect of MPL, this study applies the Carman-Kozeny equation for calculating the permeability of MPL. Permeability of cMPL made of carbon particles is calculated by [41]:

$$k_{abs,cMPL} = \frac{d_p^2 \varepsilon^3}{180(1-\varepsilon)^2} \tag{14}$$

where d_p is the particle diameter of cMPL.

The fMPL is made of randomly packed carbon nanofibers and stacked layer by layer. Permeability of the fMPL is given by the modified Carman-Kozeny equation for fiber-based porous media [42]:

$$k_{abs,fMPL} = \frac{d_f^2 \varepsilon^3}{16 k_{ck}(1-\varepsilon)^2} \tag{15}$$

where d_f is the fiber diameter of fMPL, k_{ck} is the dimensionless Carman-Kozeny constant, which can be given by [43,44]:

$$k_{ck} = \frac{2\varepsilon^3}{(1-\varepsilon)[\ln\frac{1}{1-\varepsilon} - \frac{1-(1-\varepsilon)^2}{1+(1-\varepsilon)^2}]} \tag{16}$$

2.3. Electrochemical kinetics

Electron and proton conservation equations are given for calculating electrode potential and electrolyte potential [45]:

$$0 = \nabla \cdot \left(\kappa_e^{eff} \nabla \phi_s\right) - j_e \tag{17}$$

$$0 = \nabla \cdot \left(\kappa_p^{eff} \nabla \phi_e\right) + j_p \tag{18}$$

where ϕ_s is the potential of electrodes, κ_e^{eff} is the effective electronic conductivity, j_e is the current density, ϕ_e is the potential of ionomer electrolyte, κ_p^{eff} is the effective proton conductivity, j_p is the proton flux.

Overpotential of electrochemical reaction is defined as:

$$\eta = \phi_s - \phi_e - E_{eq} \tag{19}$$

where E_{eq} is the equilibrium potential of electrochemical reaction, including oxygen reduction reaction (ORR) and hydrogen oxidation reaction (HOR).

To calculate the electrochemical reaction rate in the cathode catalyst layers, this study applies the agglomerate model, which is recognized to capture the effects of Pt/C agglomerates [39]. The reaction rate of ORR in the cathode is defined as:

$$J_{c,agg} = 4F \frac{P_{O_2}}{H_{O_2,ion}} \left[\frac{1}{E_{agg} k_c (1-\varepsilon)} + \frac{r_{agg}^2 \delta_{agg}}{3(r_{agg} + \delta_{agg}) D_{O_2,ion}} \right]^{-1} \tag{20}$$

where F is the Faraday's constant, $H_{O_2,ion}$ is the Henry's constant, r_{agg} is the radius of the agglomerate, δ_{agg} is the thickness of ionomer outside the agglomerate, $D_{O_2,ion}$ is the oxygen diffusivity in the ionomer.

The effectiveness factor of the agglomerate (E_{agg}) is defined as:

$$E_{agg} = \frac{1}{\phi_L} \left(\frac{1}{\tanh(3\phi_L)} - \frac{1}{3\phi_L} \right) \tag{21}$$

where ϕ_L is Thiele's modulus, which is defined as the ratio of reaction rate and diffusivity:

$$\phi_L = \frac{r_{agg}}{3} \sqrt{\frac{k_c}{D_{O_2,ion}}} \tag{22}$$

The oxygen reduction reaction rate of agglomerate in the cathode (k_c) is defined as:

$$k_c = \frac{A_c i_{0,ORR}^{ref}}{4FC_{O_2}^{ref}}(1-\theta_{\mathrm{PtO}})\exp\left(-\frac{\alpha_c}{RT}F\eta_c - \frac{\omega\theta_{\mathrm{PtO}}}{RT}\right)\exp\left(-7900(\frac{1}{T}-\frac{1}{353.15})\right) \quad (23)$$

where the Pt-oxide-coverage-dependent kinetics equation is applied [45,46]. Noted that θ_{PtO} is the Pt-oxide coverage, ω is the energy parameter for the Temkin isotherm. A_c is the specific surface area of active sites in the cathode catalyst layer, $C_{O_2}^{ref}$ is the reference oxygen concentration for ORR, and $i_{0,ORR}^{ref}$ is the reference exchange current density for ORR.

In the anode catalyst layer, a simplified Butler-Volmer equation is applied to calculate the electrochemical reaction rate of hydrogen oxidation,

$$J_a = A_a i_{0,HOR}^{ref}\left(\frac{C_{H_2,a}}{C_{H_2}^{ref}}\right)^{\gamma_a}\exp\left(\frac{\alpha_a}{RT}F\eta_a\right) \quad (24)$$

where A_a is the specific surface area of active sites in the anode catalyst layer, $C_{H_2}^{ref}$ is the reference hydrogen concentration for HOR, γ_a is the reaction order, and $i_{0,HOR}^{ref}$ is the reference exchange current density for HOR. Physical properties are given in Table 3.

Table 3 Physical properties.

Parameters	Expression	Ref.
Water saturation pressure [Pa]	$p_{sat} = exp(23.1963 - \frac{3816.44}{T-46.13})$	[40]
Proton conductivity of membrane [S m^{-1}]	$\kappa_{ion} = (0.5139\lambda - 0.326)\exp[1268(1/303.15 - 1/T)]$	[39]
Viscosity of liquid water [m Pa s]	$\mu = \exp(-3.63148 + \frac{542.05}{T-144.15})$	[38]
Binary diffusion coefficient [m^2 s^{-1}]	$D_{H_2H_2O} = 0.915\times10^{-4}(T/307.1)^{1.5}$ $D_{O_2N_2} = 0.22\times10^{-4}(T/293.2)^{1.5}$ $D_{O_2H_2O} = 0.282\times10^{-4}(T/308.1)^{1.5}$	[47]

	$D_{H_2ON_2} = 0.256\times10^{-4}(T/307.5)^{1.5}$	
Temperature [℃]	$T_c = T_a = 70$	[23]
Relative humidity [-]	$RH_c = RH_a = 100\%$	[23]
Reference oxygen concentration [mol m^{-3}]	$C_{O_2}^{ref} = 3.39$	[39]
	$C_{H_2}^{ref} = 56.4$	[39]
Reference exchange current density [A cm^{-2}]	$i_{0,ORR}^{ref} = 2\times10^{-5}$	[45]
	$i_{0,HOR}^{ref} = 0.27$	[37]
Agglomerate radius [μm]	$r_{agg} = 0.4$	Assumed
Ionomer thickness [μm]	$\delta_{agg} = 0.1$	Assumed

2.4. Boundary conditions

Boundary conditions are set according to experimental operating conditions in Ref. [23]. For two-phase mass transport in porous media, molar fraction of gas species and pressure are applied as the inlet boundaries at BL/channel interfaces.

Cathode $$x_{O_2,in} = 0.21(1-x_{H_2O,in}),\ x_{H_2O,in} = p_{sat}RH / p_C \quad (25)$$

Anode $$x_{H_2,in} = 1-x_{H_2O,in},\ x_{H_2O,in} = p_{sat}RH / p_A \quad (26)$$

For electrochemical reactions in PEMFCs, potentials are applied at the BL/rib interfaces.

Cathode $$\phi_s = E_{cell} \quad (27)$$

Anode $$\phi_s = 0 \quad (28)$$

Periodic boundary conditions are applied to the top and bottom symmetry boundaries shown in Fig. 1c.

$$\frac{\partial x_i}{\partial n} = 0,\ \frac{\partial p_i}{\partial n} = 0,\ \frac{\partial \phi_s}{\partial n} = 0,\ \frac{\partial \phi_e}{\partial n} = 0 \quad (29)$$

2.5. Numerical procedures

The governing equations were solved by finite element method implemented in the commercial software COMSOL Multiphysics® 5.6. The source terms and physical properties were implemented in user-defined in-built functions. Mesh of the 2D computational domains was created by mapping method. Edge mesh was first built in the bottom line in X direction, and refined in thin components (i.e., PEM, CLs, and MPLs). Sweeping method was then applied in Y directions to obtain the quadrilateral mesh with a proper aspect ratio as illustrated in Fig. 1c. Mesh of was refined and confirmed by the mesh independence study to ensure the high quality of mesh and the accuracy of simulation results in Fig. S1 in the supplementary materials. Simulations were completed with the workstation with 12 processors (Intel® Xeon® CPU E5-2680 v3 @ 2.50GHz).

3. Results and discussion

3.1. Validation

The numerical model was first validated against the experimental results of PEMFCs with cMPL and fMPL using polarization curves. Except for the type of MPL, simulation and experiments of PEMFCs with cMPL and fMPL were conducted with identical cell configurations and under the same operating conditions. As shown in Fig. 2, the numerical results of PEMFCs with cMPL and fMPL are in good agreement with the experimental data, suggesting the accuracy of our modeling in reproducing the physiochemical processes of the PEMFCs. It is found that the PEMFCs with cMPL and fMPL show similar activation and ohmic polarizations. Significant concentration loss is observed in the PEMFC with cMPL under high current densities, indicating that PEMFC with cMPL suffer from insufficient oxygen supply and water flooding. In contrast, fMPL enables PEMFC to achieve a much higher

limiting current density, which is ascribed to the enhanced mass transport and water removal due to the higher porosity and permeability of fMPL.

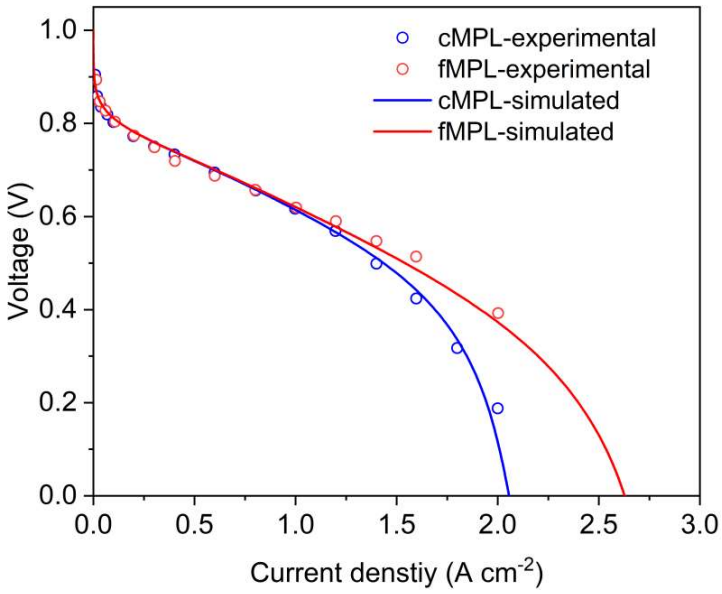

Fig. 2. Validation of the model against the experimental results of PEMFCs with cMPL and fMPL [23].

3.2. Comparison between cMPL of fMPL

To better understand the effect of MPL on cell performance, the saturation and oxygen concentration were calculated. As can be seen in Fig. 3a, liquid water saturation in CL and MPL of PEMFC with fMPL is significantly lower than that with cMPL at the same current density of 2 A cm^{-2}, indicating better water removal capability of fMPL. This can be ascribed to the higher permeability of fMPL in the through-plane direction. It should be noted that the difference of liquid water saturation in BL is less significant, due to the high permeability of BL. As shown in Fig. 3b, the oxygen concentration of PEMFC with fMPL is higher than that with cMPL, which can result in better cell performance. Moreover, it can be found that the oxygen concentration of PEMFC with cMPL drops dramatically from BL to CL, indicating much higher oxygen transport resistance.

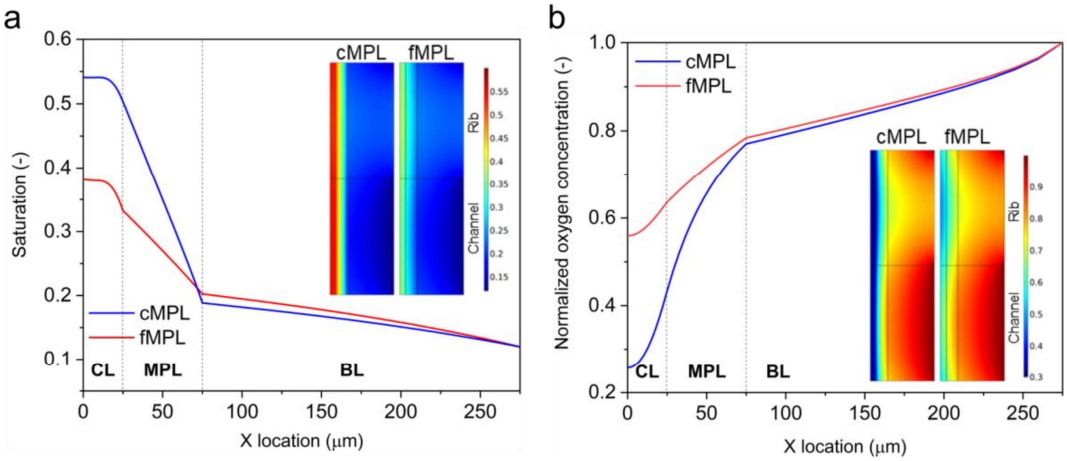

Fig. 3. Comparison between cMPL and fMPL. (a) Saturation distribution and (b) Oxygen concentration distribution.

Fig. 4 compares the vapor water fraction, ionomer water content, and water flux in PEMFCs with fMPL and cMPL. It can be found that the water vapor fraction of PEMFC with cMPL in the cathode is much higher than that with fMPL due to the relatively poor drainage capability, while the vapor water fraction in the anode is similar, as shown in Fig. 4a. In addition, the ionomer water content of PEMFC with fMPL (Fig. 4b) is higher than that of cMPL in anode CL, PEM, and most parts of cathode CL, representing better membrane hydration, which leads to a higher proton conductivity and smaller ohmic loss. The effect of MPL on water flux (driven by back diffusion and electro-osmosis) across the PEM is displayed in Fig. 4c. At 100% RH and 2 A cm^{-2}, for both fMPL and cMPL, the absolute value of electro-osmosis flux is larger than back diffusion flux, indicating that the net water flux across PEM is from anode to cathode. It means that in addition to water generated by ORR, net water flux across PEM also contributes to water accumulation in cathode CL. Therefore, it is crucial to drain these water sources from cathode CL to cathode channels to avoid water flooding. Particularly, the back diffusion of PEMFC with cMPL is higher than that of fMPL, which is consistent with the higher vapor water fraction observed in the cathode of PEMFC with cMPL. In the meantime, the electro-osmosis-driven water flux of PEMFC with cMPL is also higher than that of fMPL, which can

be ascribed to the higher electrolyte potential (ϕ_e) of PEMFC with cMPL, as the operating voltage of PEMFC with cMPL is lower at an identical high current density.

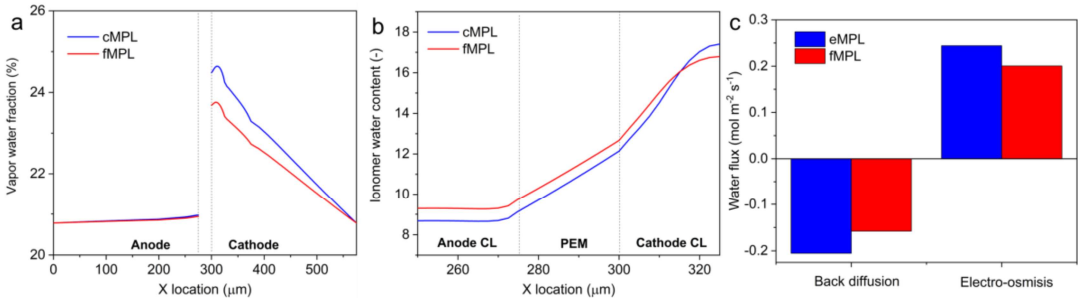

Fig. 4. Comparison between cMPL and fMPL. (a) Vapor water fraction, (b) Ionomer water content, and (c) Water flux. Note that positive flux is from anode to cathode, while negative flux is from anode to cathode.

Fig. 5a displays the polarization curves of PEMFCs with cMPL and fMPL at different temperatures. Under the investigated temperatures from 40 to 80 ℃, PEMFC with cMPL shows better performance than that with cMPL, especially under high current densities. Moreover, both the PEMFCs with cMPL and fMPL exhibit inferior performance at lower operating temperatures owing to the higher activation and concentration polarization. The former is caused by the reduced catalytic activity while the latter resulting from higher liquid water saturation due to reduced saturated pressure of water. As shown in Fig. 5b, when the temperature is reduced from 80 to 40 ℃, the average saturation of cathode CL is increased by 32.2% and 36.6% for PEMFCs with cMPL and fMPL, respectively. The higher liquid water saturation will increase oxygen transport resistance, which is a typical parameter to describe the transport characteristics [48]. For both types of MPL, a decrease in temperature leads to a dramatic increase in oxygen transport resistance, especially for PEMFC with cMPL, as depicted in Fig. 5c. Specifically, when the temperature is reduced from 80 to 40 ℃, oxygen transport resistance is increased by 174.3% to 101.8 s m^{-1} for PEMFC with cMPL and 110.4%

to 38.9 s m^{-1} for PEMFC with fMPL. The simulation results agree well with experimental results of oxygen transport resistance in Ref. [23].

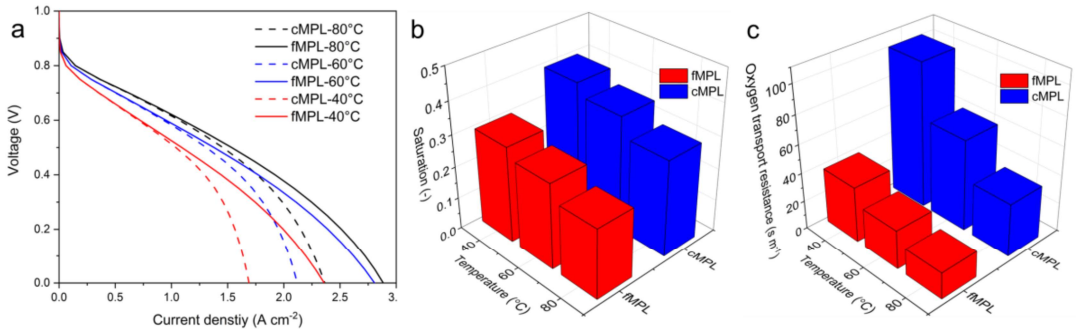

Fig. 5. Comparison between cMPL and fMPL at different temperatures. (a) Polarization curves, (b) Liquid water saturation, and (c) Oxygen transport resistances.

3.3. Effect of porosity

As the transitional layer between CL and BL, the porosity of MPL should be higher than that of CL to drain water out effectively while smaller than that of BL to avoid the CL nanoparticles dripping into BL and ensure good interfacial contact and keep high bulk electron conductivity [6]. Typically, the porosity of CL and BL are around 0.3 and 0.7, respectively [49]. Therefore, in this work, the effect of fMPL porosity on PEMFC performance was studied by varying the porosity from 0.3 to 0.7. As shown in Fig. 6a, with the increase of fMPL porosity, PEMFCs achieve a higher limiting current density, which is attributed to the decrease in concentration loss. The increase in PEMFC power density becomes less evident when the porosity is raised above 0.5, as seen from the inset, implying that the porosity above 0.5 (and below 0.7) is suitable for fMPL fabrication in PEMFC. The reduced concentration loss with the increase of fMPL porosity can be attributed to the reduced liquid saturation in CL, MPL, and BL (Fig. 6b), which reduces the oxygen transport resistance. It should be pointed out that fMPL with a porosity above 0.5 can be easily fabricated by controlling the fiber density by adjusting the electrospinning conditions (e.g., rotating rate and feeding rate) or post-treatment [50].

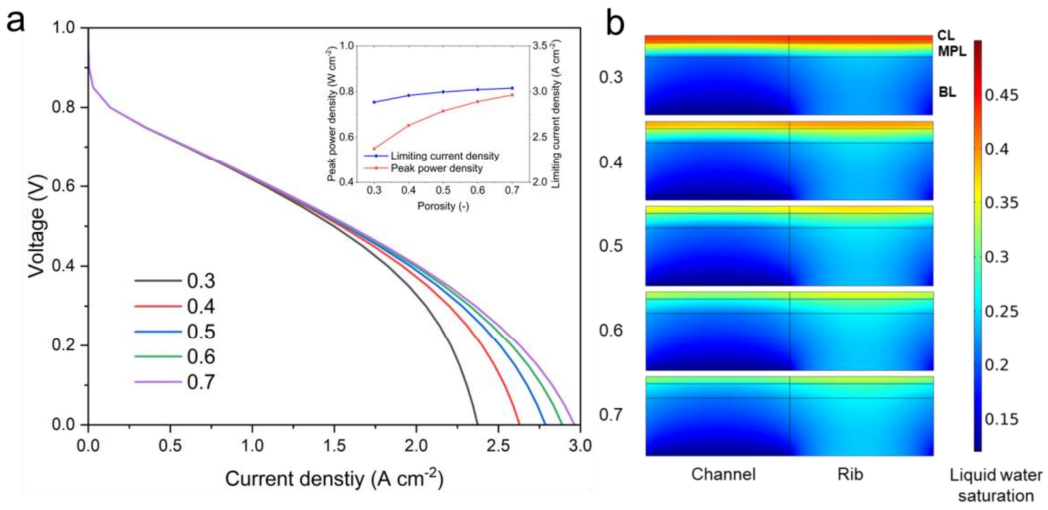

Fig. 6. Effects of porosity of fMPL on (a) Cell performance and (b) Saturation distribution.

3.4. Effect of fiber diameter

Fiber diameter is another important structural property of fMPL that influences the permeability of the porous material. Typically, the diameter of electrospun carbon fibers is of nano- and micro-scale [51]. Therefore, different fiber diameters, i.e., 0.5, 1, 2, 4, 6, and 8 μm were selected to study the effect of fMPL fiber diameter on PEMFC performance. As shown in Fig. 7a, due to the increased permeability of fMPL with increased fiber diameter, the concentration loss of PEMFC is reduced accordingly, enabling increased limiting current density. However, when the fiber diameter is larger than 2 μm, the improvement in PEMFC performance becomes less significant. Meanwhile, it should be noted that the electrospinning process becomes unstable when fabricating fibers with a larger fiber diameter [52]. In practical application, a fiber diameter of ~2 μm can be adopted for ease of fabrication. Conventionally, the fiber diameter of electrospun carbon fibers can be increased by increasing the concentration of precursor solutions. For example, the fMPL with a fiber diameter of around 2 μm can be fabricated with 18 wt% polyacrylonitrile (PAN) precursor [53]. Fig. 7b reveal that the

enhancement in PEMFC performance is attributed to the significant reduction of liquid water saturation in CL, MPL, and BL when the fiber diameter is increased from 0.5 to 2 μm.

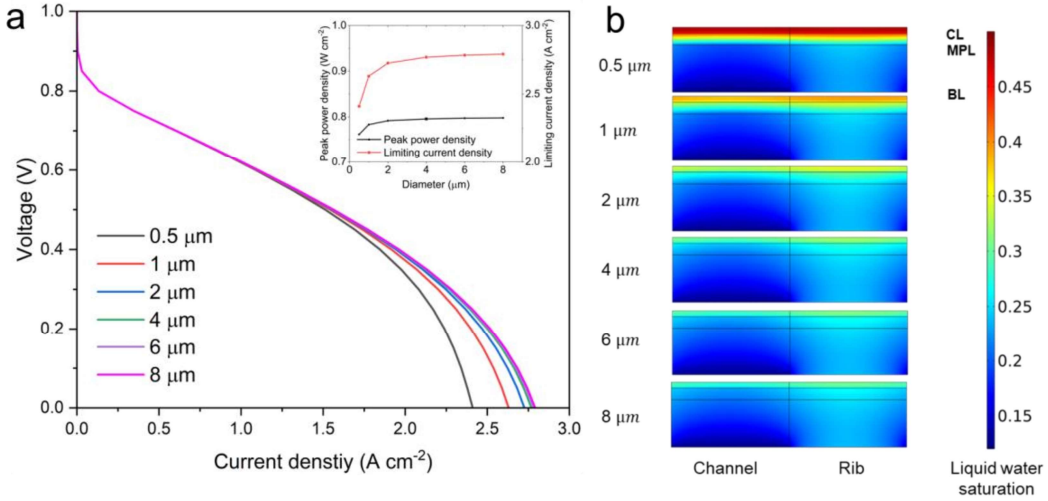

Fig. 7. Effects of fiber diameter of fMPL on (a) Cell performance and (b) Saturation distribution.

3.5. Effect of hydrophilicity

In addition to the structural parameters, the hydrophilicity of MPL also has a significant effect on the cell performance. Fig. 8a depicts the polarization curves of PEMFCs with a fMPL of various hydrophilicity. It is found that contact angle of 95° results in a large concentration loss, with which the PEMFC can only achieve a small limiting current density 1.40 A cm^{-2}. By increasing the hydrophobicity of fMPL, the performance of the PEMFCs is effectively improved. As can be seen in Fig. 8b, the improved cell performance is due to facilitated oxygen transport as a result of reduced liquid water saturation in CL, MPL and BL. The limiting current density is dramatically increased to 2.63 A cm^{-2} when the contact angle of fMPL is increased from 95 to 135°, but further increase in hydrophobicity of fMPL shows limited performance enhancement. Hence, it is suggested that the contact angle of fMPL should be no less than 135°.

In real applications, the hydrophilicity of fMPL can adjusted by PTFE treatment or adjusting

the precursor and controlling the post-treatment conditions. For example, higher carbonization temperature can increase the graphitization degree of electrospun carbon fiber and improve the hydrophobicity of the fMPL [54].

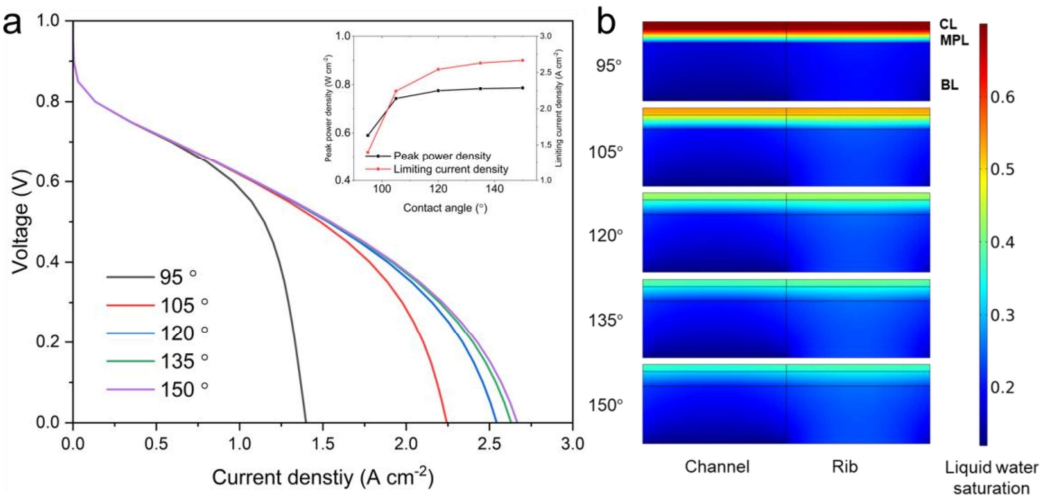

Fig. 8. Effects of contact angle of fMPL on (a) Cell performance and (b) Saturation distribution.

4. Conclusion

In summary, a two-phase multi-physics model was successfully developed for PEMFCs with fiber-based MPL. In this study, water transport in porous media, membrane and ionomer was considered. Carman-Kozeny equations were applied to calculate the permeability of cMPL and fMPL. The simulation agrees well with the experimental results of PEMFCs with cMPL and fMPL. Based on this model, the effects of types of MPL and key parameters of fMPL including porosity, fiber diameter, and hydrophobicity on the cell performance were investigated. Key findings are summarized as follows. A remarkable increase in cell performance is achieved when applying fMPL, especially under high current density. fMPL enables better water removal capability and oxygen transport capability, resulting in lower liquid water saturation and higher oxygen concentration. In addition, fMPL can reduce the vapor water fraction in the cathode markedly and maintain high ionomer water content. The net water flux across PEM is

from anode to cathode, emphasizing the importance of water drainage from cathode CL to cathode channel to avoid water flooding. Moreover, PEMFCs with fMPL show better performance than that with cMPL under a wide operating temperature range (from 40 to 80 ℃), which is due to lower liquid water saturation and oxygen transport resistance. Furthermore, the parametric study suggested that fMPL with a porosity above 0.5, fiber diameter above 2 μm, and contact angle above 135° can effectively enhance the water removal capability and thus improve the cell performance.

Acknowledgment

The work described in this paper was supported by HKUST Fund of Foshan (Grant No. FSUST19-FYTRI06) and a grant from the Research Grants Council of the Hong Kong Special Administrative Region, China (Grant No. HKUST C6011-20G).

References

[1] K. Jiao, J. Xuan, Q. Du, Z. Bao, B. Xie, B. Wang, Y. Zhao, L. Fan, H. Wang, Z. Hou, others, Designing the next generation of proton-exchange membrane fuel cells, Nature. 595 (2021) 361–369.
[2] Y. Wang, J. Liao, Z. Li, B. Wu, J. Lou, L. Zeng, T. Zhao, Ir-Pt/C composite with high metal loading as a high-performance anti-reversal anode catalyst for proton exchange membrane fuel cells, Int. J. Hydrog. Energy. 47 (2022) 13101–13111.
[3] W. Gu, M. Wu, J. Xu, T. Zhao, MXene boosted metal-organic framework-derived Fe–N–C as an efficient electrocatalyst for oxygen reduction reactions, Int. J. Hydrog. Energy. 47 (2022) 17224–17232.
[4] F. Xiao, Q. Wang, G.-L. Xu, X. Qin, I. Hwang, C.-J. Sun, M. Liu, W. Hua, H. Wu, S. Zhu, others, Atomically dispersed Pt and Fe sites and Pt–Fe nanoparticles for durable proton exchange membrane fuel cells, Nat. Catal. (2022) 1–10.
[5] M.A. Hickner, N.P. Siegel, K.S. Chen, D.S. Hussey, D.L. Jacobson, M. Arif, Understanding liquid water distribution and removal phenomena in an operating PEMFC via neutron radiography, J. Electrochem. Soc. 155 (2008) B294.
[6] P.C. Okonkwo, C. Otor, A review of gas diffusion layer properties and water management in proton exchange membrane fuel cell system, Int. J. Energy Res. 45 (2021) 3780–3800.
[7] Y. Yang, X. Zhou, B. Li, C. Zhang, Recent progress of the gas diffusion layer in proton exchange membrane fuel cells: Material and structure designs of microporous layer, Int. J. Hydrog. Energy. 46 (2021) 4259–4282.
[8] A. Ozden, S. Shahgaldi, X. Li, F. Hamdullahpur, A review of gas diffusion layers for proton exchange membrane fuel cells—With a focus on characteristics, characterization techniques, materials and designs, Prog. Energy Combust. Sci. 74 (2019) 50–102.

[9] J. Zhang, B. Wang, J. Jin, S. Yang, G. Li, A review of the microporous layer in proton exchange membrane fuel cells: Materials and structural designs based on water transport mechanism, Renew. Sustain. Energy Rev. 156 (2022) 111998.
[10] Y. Nagai, J. Eller, T. Hatanaka, S. Yamaguchi, S. Kato, A. Kato, F. Marone, H. Xu, F.N. Büchi, Improving water management in fuel cells through microporous layer modifications: Fast operando tomographic imaging of liquid water, J. Power Sources. 435 (2019) 226809.
[11] A. Forner-Cuenca, J. Biesdorf, L. Gubler, P.M. Kristiansen, T.J. Schmidt, P. Boillat, Engineered water highways in fuel cells: radiation grafting of gas diffusion layers, Adv. Mater. 27 (2015) 6317–6322.
[12] D. Spernjak, R. Mukundan, R.L. Borup, L.G. Connolly, B.I. Zackin, V. De Andrade, M. Wojcik, D.Y. Parkinson, D.L. Jacobson, D.S. Hussey, others, Enhanced water management of polymer electrolyte fuel cells with additive-containing microporous layers, ACS Appl. Energy Mater. 1 (2018) 6006–6017.
[13] T. Kitahara, H. Nakajima, K. Mori, Hydrophilic and hydrophobic double microporous layer coated gas diffusion layer for enhancing performance of polymer electrolyte fuel cells under no-humidification at the cathode, J. Power Sources. 199 (2012) 29–36.
[14] Y. Hou, X. Li, Q. Du, K. Jiao, N. Zamel, Pore-scale investigation of the effect of micro-porous layer on water transport in proton exchange membrane fuel cell, J. Electrochem. Soc. 167 (2020) 144504.
[15] A.Z. Weber, J. Newman, Effects of Microporous Layers in Polymer Electrolyte Fuel Cells, J. Electrochem. Soc. 152 (2005) A677.
[16] M. Sarker, M.A. Rahman, F. Mojica, S. Mehrazi, W.J. Kort-Kamp, P.-Y.A. Chuang, Experimental and computational study of the microporous layer and hydrophobic treatment in the gas diffusion layer of a proton exchange membrane fuel cell, J. Power Sources. 509 (2021) 230350.
[17] C.-C. Fan, M.-H. Chang, Improving proton exchange membrane fuel cell performance with carbon nanotubes as the material of cathode microporous layer, Int. J. Energy Res. 40 (2016) 181–188.
[18] J. Lee, R. Banerjee, M. George, D. Muirhead, P. Shrestha, H. Liu, N. Ge, S. Chevalier, A. Bazylak, Multiwall carbon nanotube-based microporous layers for polymer electrolyte membrane fuel cells, J. Electrochem. Soc. 164 (2017) F1149.
[19] R. Schweiss, M. Steeb, P.M. Wilde, T. Schubert, Enhancement of proton exchange membrane fuel cell performance by doping microporous layers of gas diffusion layers with multiwall carbon nanotubes, J. Power Sources. 220 (2012) 79–83.
[20] A. Ozden, S. Shahgaldi, X. Li, F. Hamdullahpur, A graphene-based microporous layer for proton exchange membrane fuel cells: characterization and performance comparison, Renew. Energy. 126 (2018) 485–494.
[21] Q. Duan, B. Wang, J. Wang, H. Wang, Y. Lu, Fabrication of a carbon nanofiber sheet as a micro-porous layer for proton exchange membrane fuel cells, J. Power Sources. 195 (2010) 8189–8193.
[22] M. Balakrishnan, P. Shrestha, N. Ge, C. Lee, K.F. Fahy, R. Zeis, V.P. Schulz, B.D. Hatton, A. Bazylak, Designing Tailored Gas Diffusion Layers with Pore Size Gradients via Electrospinning for Polymer Electrolyte Membrane Fuel Cells, ACS Appl. Energy Mater. 3 (2020) 2695–2707.
[23] C. Li, D. Si, Y. Liu, J. Zhang, Y. Liu, Water management characteristics of electrospun micro-porous layer in PEMFC under normal temperature and cold start conditions, Int. J. Hydrog. Energy. 46 (2021) 11150–11159. https://doi.org/10.1016/j.ijhydene.2020.05.271.
[24] M. Inagaki, Y. Yang, F. Kang, Carbon Nanofibers Prepared via Electrospinning, Adv. Mater. 24 (2012) 2547–2566.

[25] A.Z. Weber, R.L. Borup, R.M. Darling, P.K. Das, T.J. Dursch, W. Gu, D. Harvey, A. Kusoglu, S. Litster, M.M. Mench, others, A critical review of modeling transport phenomena in polymer-electrolyte fuel cells, J. Electrochem. Soc. 161 (2014) F1254.
[26] N. Ge, S. Chevalier, J. Lee, R. Yip, R. Banerjee, M.G. George, H. Liu, C. Lee, M. Fazeli, P. Antonacci, T. Kotaka, Y. Tabuchi, A. Bazylak, Non-isothermal two-phase transport in a polymer electrolyte membrane fuel cell with crack-free microporous layers, Int. J. Heat Mass Transf. 107 (2017) 418–431.
[27] Y. Xu, R. Fan, G. Chang, S. Xu, T. Cai, Investigating temperature-driven water transport in cathode gas diffusion media of PEMFC with a non-isothermal, two-phase model, Energy Convers. Manag. 248 (2021) 114791.
[28] J. Zhou, S. Shukla, A. Putz, M. Secanell, Analysis of the role of the microporous layer in improving polymer electrolyte fuel cell performance, Electrochimica Acta. 268 (2018) 366–382.
[29] C. Csoklich, M. Sabharwal, T.J. Schmidt, F.N. Büchi, Does the thermal conductivity of gas diffusion layer matter in polymer electrolyte fuel cells?, J. Power Sources. 540 (2022) 231539.
[30] K.N. Kim, J.H. Kang, S.G. Lee, J.H. Nam, C.-J. Kim, Lattice Boltzmann simulation of liquid water transport in microporous and gas diffusion layers of polymer electrolyte membrane fuel cells, J. Power Sources. 278 (2015) 703–717.
[31] T. Jahnke, G. Futter, A. Latz, T. Malkow, G. Papakonstantinou, G. Tsotridis, P. Schott, M. Gérard, M. Quinaud, M. Quiroga, others, Performance and degradation of Proton Exchange Membrane Fuel Cells: State of the art in modeling from atomistic to system scale, J. Power Sources. 304 (2016) 207–233.
[32] A.R. Kalidindi, R. Taspinar, S. Litster, E.C. Kumbur, A two-phase model for studying the role of microporous layer and catalyst layer interface on polymer electrolyte fuel cell performance, Int. J. Hydrog. Energy. 38 (2013) 9297–9309.
[33] P.Z. Lin, J. Sun, M.C. Wu, T.S. Zhao, A multiscale model for proton exchange membrane fuel cells with order-structured catalyst layers, Int. J. Heat Mass Transf. 195 (2022) 123092.
[34] L. Fan, G. Zhang, K. Jiao, Characteristics of PEMFC operating at high current density with low external humidification, Energy Convers. Manag. 150 (2017) 763–774.
[35] J. Liang, Y. Li, R. Wang, J. Jiang, Cross-dimensional model of the oxygen transport behavior in low-Pt proton exchange membrane fuel cells, Chem. Eng. J. 400 (2020) 125796.
[36] F.C. Cetinbas, X. Wang, R.K. Ahluwalia, N.N. Kariuki, R.P. Winarski, Z. Yang, J. Sharman, D.J. Myers, Microstructural Analysis and Transport Resistances of Low-Platinum-Loaded PEFC Electrodes, J. Electrochem. Soc. 164 (2017) F1596.
[37] R. Vetter, J.O. Schumacher, Experimental parameter uncertainty in proton exchange membrane fuel cell modeling. Part I: Scatter in material parameterization, J. Power Sources. 438 (2019) 227018.
[38] R. Vetter, J.O. Schumacher, Free open reference implementation of a two-phase PEM fuel cell model, Comput. Phys. Commun. 234 (2019) 223–234.
[39] G. Zhang, J. Wu, Y. Wang, Y. Yin, K. Jiao, Investigation of current density spatial distribution in PEM fuel cells using a comprehensively validated multi-phase non-isothermal model, Int. J. Heat Mass Transf. 150 (2020) 119294.
[40] W.W. Yang, T.S. Zhao, A two-dimensional, two-phase mass transport model for liquid-feed DMFCs, Electrochimica Acta. 52 (2007) 6125–6140.
[41] J. Bear, Dynamics of fluids in porous media, Courier Corporation, 1988.

[42] O. Rahli, L. Tadrist, M. Miscevic, R. Santini, Fluid Flow Through Randomly Packed Monodisperse Fibers: The Kozeny-Carman Parameter Analysis, J. Fluids Eng. 119 (1997) 188–192.
[43] J. Sun, H.R. Jiang, M.C. Wu, X.Z. Fan, C.Y.H. Chao, T.S. Zhao, A novel electrode formed with electrospun nano- and micro-scale carbon fibers for aqueous redox flow batteries, J. Power Sources. 470 (2020) 228441.
[44] J. Sun, H.R. Jiang, B.W. Zhang, C.Y.H. Chao, T.S. Zhao, Towards uniform distributions of reactants via the aligned electrode design for vanadium redox flow batteries, Appl. Energy. 259 (2020) 114198.
[45] L. Hao, K. Moriyama, W. Gu, C.-Y. Wang, Modeling and experimental validation of Pt loading and electrode composition effects in PEM fuel cells, J. Electrochem. Soc. 162 (2015) F854.
[46] N.P. Subramanian, T.A. Greszler, J. Zhang, W. Gu, R. Makharia, Pt-oxide coverage-dependent oxygen reduction reaction (ORR) kinetics, J. Electrochem. Soc. 159 (2012) B531.
[47] Fuel Cell & Electrolyzer Module User's Guide. COMSOL Multiphysics® v. 5.6. COMSOL AB, Stockholm, Sweden. 2021, (n.d.).
[48] N. Nonoyama, S. Okazaki, A.Z. Weber, Y. Ikogi, T. Yoshida, Analysis of oxygen-transport diffusion resistance in proton-exchange-membrane fuel cells, J. Electrochem. Soc. 158 (2011) B416.
[49] I.V. Zenyuk, P.K. Das, A.Z. Weber, Understanding impacts of catalyst-layer thickness on fuel-cell performance via mathematical modeling, J. Electrochem. Soc. 163 (2016) F691.
[50] J. Xue, T. Wu, Y. Dai, Y. Xia, Electrospinning and Electrospun Nanofibers: Methods, Materials, and Applications, Chem. Rev. 119 (2019) 5298–5415.
[51] R. Ruiz-Rosas, J. Bedia, M. Lallave, I.G. Loscertales, A. Barrero, J. Rodríguez-Mirasol, T. Cordero, The production of submicron diameter carbon fibers by the electrospinning of lignin, Carbon. 48 (2010) 696–705.
[52] J. Sun, M. Wu, H. Jiang, X. Fan, T. Zhao, Advances in the design and fabrication of high-performance flow battery electrodes for renewable energy storage, Adv. Appl. Energy. 2 (2021) 100016.
[53] L. Zeng, J. Sun, T.S. Zhao, Y.X. Ren, L. Wei, Balancing the specific surface area and mass diffusion property of electrospun carbon fibers to enhance the cell performance of vanadium redox flow battery, Int. J. Hydrog. Energy. 45 (2020) 12565–12576.
[54] J. Zhu, S. Zhang, L. Wang, D. Jia, M. Xu, Z. Zhao, J. Qiu, L. Jia, Engineering cross-linking by coal-based graphene quantum dots toward tough, flexible, and hydrophobic electrospun carbon nanofiber fabrics, Carbon. 129 (2018) 54–62.

Declaration of interests

☒ The authors declare that they have no known competing financial interests or personal relationships that could have appeared to influence the work reported in this paper.

☐The authors declare the following financial interests/personal relationships which may be considered as potential competing interests:

CRediT author statement

P.Z. Lin: Conceptualization, Methodology, Formal analysis, Writing -original draft, Writing-review and Editing. **J. Sun:** Conceptualization, Methodology, Formal analysis, Writing -original draft, Writing-review and Editing. **M. H. Shao**: Resources, Writing-review and editing, Project administration. **M.C. Wu:** Methodology, Formal analysis, Writing-review and Editing. **T.S. Zhao**: Resources, Writing-review and editing, Supervision, Project administration.